

Fast-neutron induced pre-equilibrium reactions on ^{55}Mn and $^{63,65}\text{Cu}$ at energies up to 40 MeV

M. Avrigeanu^a, S.V. Chuvaev^b, A.A. Filatenkov^b,
R.A. Forrest^c, M. Herman^d, A.J. Koning^e, A.J.M. Plompen^f,
F.L. Roman^a, V. Avrigeanu^{a,*}

^a*"Horia Hulubei" National Institute for Physics and Nuclear Engineering, P.O. Box MG-6, 077125 Bucharest, Romania*

^b*V.G. Khlopin Radium Institute, 2nd Murinski Ave. 28, St. Petersburg 194021, Russia*

^c*EURATOM-UKAEA Fusion Association, Culham Science Centre, Abingdon OX14 3DB, United Kingdom*

^d*Brookhaven National Laboratory, P.O. Box 5000, Upton, NY 11973-5000*

^e*Nuclear Research and Consultancy Group NRG, P.O. Box 25, 1755 ZG Petten, The Netherlands*

^f*European Commission, Joint Research Center, Institute for Reference Materials and Measurements, B-2440 Geel, Belgium*

Abstract

Excitation functions were measured for the $^{55}\text{Mn}(n,2n)^{54}\text{Mn}$, $^{55}\text{Mn}(n,\alpha)^{52}\text{V}$, $^{63}\text{Cu}(n,\alpha)^{60}\text{Co}$, $^{65}\text{Cu}(n,2n)^{64}\text{Cu}$, and $^{65}\text{Cu}(n,p)^{65}\text{Ni}$ reactions from 13.47 to 14.83 MeV. The experimental cross sections are compared with the results of calculations including all activation channels for the stable isotopes of Mn and Cu, for neutron incident energies up to 50 MeV. Within the energy range up to 20 MeV the model calculations are most sensitive to the parameters related to nuclei in the early stages of the reaction, while the model assumptions are better established by analysis of the data in the energy range 20–40 MeV. While the present analysis has taken advantage of both a new set of accurate measured cross sections around 14 MeV and the larger data basis fortunately available between 20 and 40 MeV for the Mn and Cu isotopes, the need of additional measurements below as well as above 40 MeV is pointed out.

Key words: ^{55}Mn , $^{63,65}\text{Cu}$, $E \leq 40$ MeV, Neutron activation cross section measurements, Nuclear reactions, Model calculations, Manganese, Copper
PACS: 24.10.-I, 24.60.Dr, 25.40.-h, 28.20.-v

1 Introduction

As part of a general investigation [1,2,3,4] of the reaction mechanisms of fast neutrons at low and medium energies, we have analyzed the activation cross sections of the odd-mass isotopes ^{55}Mn and $^{63,65}\text{Cu}$ in the excitation-energy range up to 50 MeV.

The main purpose of this paper is to present new experimental results and discuss some of the question marks associated with the model calculations which combine pre-equilibrium emission (PE) with equilibrium decay of the remaining compound nucleus. Although our primary aim was to comply with the needs of a sound, complete and reliable neutron-induced cross section data library to address safety and environmental issues of the fusion programme [5,6], the analysis results also enabled a stringent test of models for the above-mentioned nuclear processes. The odd-mass target nuclei within the present work may be particularly useful in connection with the proven influence of the $f_{7/2}$ neutron and proton shell closures on the particle PE spectra (e.g., [7]). Actually Koning and Duijvestijn [8] pointed out that omission of the shell effects is probably the most important cause of the remaining discrepancies in their large-scale comparison of the nucleon PE model with angle-integrated nucleon spectra. Moreover, a systematic analysis by Mills et al. [9] in the same mass range highlighted that some of the discrepancies observed in the yields of nuclides with closed or nearly-closed nucleon shells may not affect the inherent validity of the relevant model but follow the use of incorrect, e.g., average model parameters for certain nuclei involved in the decay process. Thus, in order to gain insight into this problem, we have analyzed the activation cross sections of ^{55}Mn and $^{63,65}\text{Cu}$ isotopes using the parameter databases obtained previously by global optimization within the computer codes TALYS [10] and EMPIRE-II [11], as well as a local parameter set within the STAPRE-H code [12]. No fine tuning was done to optimize the description of the nucleon emission for all the cases, but for STAPRE-H a consistent set of local parameters has previously been established or validated on the basis of independent experimental information of, e.g., neutron total cross sections, proton reaction cross sections, low-lying level and resonance data, and γ -ray strength functions based on neutron-capture data. The comparison of various calculations, including their sensitivity to model approaches and parameters, has concerned all the activation channels for which there are measured data. It has thus avoided the use of model parameters which have been improperly adjusted to take into account properties peculiar to specific nuclei in the decay cascade, considered to be the case for discrepancies observed around the closures of both the $f_{7/2}$ proton and neutron shells [9].

* Corresponding author. Tel.: +40-21-4046125
Email address: vavrig@ifin.nipne.ro (V. Avrigeanu).

The cross sections for nuclear reactions induced by fast neutrons below 20 MeV are generally considered to be reasonably well known in spite of many fast neutron reactions for which the available data are either conflicting or incomplete even around 14 MeV. Consequently the recent set of accurately measured cross sections below 20 MeV presented in Section 2 are extremely valuable. Actually the model calculations of these data are most sensitive to the parameters related to nuclei in the early stages of the reaction, including the PE processes which then dominate at higher energies. The corresponding model assumptions are thus better investigated by analysing the data above 20–30 MeV, which helpfully exist for the stable isotopes of Mn and Cu, provided that (i) a large body of data is described with no free but consistent model parameters, properly established by the analysis of other independent data, and (ii) the statistical parameters related to nuclei in the decay cascade are validated by the account of the data below ~ 20 MeV. Thus, in order to match these former constraints, the main themes and parameters of the model calculations with the three computer codes are discussed in Section 3, while the experimental data and their comparison with the above-mentioned approaches are discussed in detail in Section 4. Finally, consideration of the main outcomes of this work is given in Section 5, the first half being additionally related to the above-mentioned analysis below ~ 20 MeV, thus making possible the focus on the discussion of model assumptions at higher energies. Preliminary results have been reported elsewhere [13,14].

2 Experimental method

The well known activation method was used in order to obtain the measured cross sections. A comprehensive overview of both the measurements carried out at the KRI Neutron Generator NG-400 and the experimental setup that was well tested in many previous measurements is given in Refs. [13,15], while we mention in the following only some basic points relevant to the present work.

Cross sections were determined by measuring the activity of samples irradiated by neutrons from the ${}^3\text{H}(\text{d},\text{n}){}^4\text{He}$ reaction, with a deuteron beam energy of 280 keV. Samples were made of tablets of pressed powder of potassium manganese KMnO_4 , and respectively thin metallic copper foils of natural abundance. They had 14 mm diameter and the weight of 1100 mg and 360 mg, respectively. The target discs were sandwiched between two niobium or two aluminum foils that were used for neutron fluence determination. Sample assemblies were located around the target at different angles to the deuteron beam, thus providing different mean neutron energies in the region of 13.4 - 14.9 MeV. The neutron energy spectrum was calculated for every sample by taking into account the real geometry of each irradiation, the reaction cross section eval-

uation of Drogg [16], and the stopping power evaluation of Anderson and Ziegler [17]. The real beam and target characteristics were also accounted for [18], and variations of the neutron flux during irradiation were registered by two independent scintillation detectors. The absolute neutron fluences accumulated by the samples were determined by using the $^{93}\text{Nb}(n,2n)^{92m}\text{Nb}$ and $^{27}\text{Al}(n,\alpha)^{24}\text{Na}$ standard cross sections. The $^{27}\text{Al}(n,\alpha)^{24}\text{Na}$ cross sections were taken from the FENDL/A-2.0 evaluation [19], while the experimental values of the $^{93}\text{Nb}(n,2n)^{92m}\text{Nb}$ cross sections, obtained in Ref. [13] relative to the same standard, were considered since these data show a smoother behavior of the cross section curve. Differences between the data of Ref. [13] and the evaluation of Ref. [20] are less than the combined errors of measurement and evaluation, and do not exceed 1.35%.

The γ -ray counting of the irradiated samples was done by means of two detectors, enclosed in passive shields. The first was a HPGe detector with a thin beryllium entrance window, and the second was a Ge(Li) detector. The HPGe detector had a relative efficiency of 24.7%, and the Ge(Li) detector had a volume of 160 cm³. The energy resolutions of the HPGe and Ge(Li) detectors were 1.8 keV and 4.0 keV, respectively, at 1332 keV. The background count rate was 0.00064 counts/(s.keV) for the HPGe detector and 0.00019 counts/(s.keV) for the Ge(Li) detector at 1300 keV. All the observable γ -ray peaks were revealed and identified in the spectra. The decay data used for cross section calculations (half-lives, γ -ray energies, and yields) were obtained from Ref. [21]. The reaction cross sections presented in Table 1 are weighted averages of cross sections obtained for every γ -ray line related to the reactions.

3 Nuclear models and calculations

3.1 Global approach

The two sets of global calculations within the direct-reaction, PE and statistical Hauser-Feshbach (HF) models, performed by means of the computer codes TALYS [10] and EMPIRE-II [11], have mainly used systematics based on global phenomenological analysis. Thus their results are firstly predictions of the reaction cross sections which should be considered from the point of view of the global parameters involved in the corresponding calculations. Actually, such blind calculations typically produce a correct shape for the excitation functions, while there is as much underprediction as overprediction when the results are compared with data for all nuclides of the periodic table of elements. Moreover, for a true evaluation, a normalization of the curves can always be performed with nuclear model parameters that have an intrinsic uncertainty, such as average radiative widths, level density parameters and pre-equilibrium

matrix elements. However, for large-scale data evaluations based on nuclear model calculations, the performance of the corresponding global estimations of these data are also quite important. The main assumptions and parameters involved in this work for both sets of global calculations have been recently described [4], while detailed descriptions were lately given [8,11] too. Therefore we give here only some specific points which have arisen in the meantime.

A similar approach using the code TALYS was applied in this work to the Mn and Cu isotopes as that reported in Refs. [2,3] for Co, Ni, and Mo isotopes. However, a new version (0.72) of the TALYS code was used although the previous description regarding the choices for the optical model potential (OMP) [22], the direct reaction (using ECIS97 [23]), the level density model [24,25] including the damping of shell effects at high excitation energies, and especially the PE contributions with the two-component Exciton model using Kalbach systematics [26] and particle-hole state densities including surface effects [27,28] which depend on the type of projectile and the target mass [8] has been not altered for calculations that were performed in this work. The discrete level schemes are adopted from the RIPL-2 database [24]. We note that for this paper TALYS was only used for the global approach. A full description of the models and methods used in TALYS can be found in Refs. [29,30,31,32], where also the applicability of the code for the local approach, i.e. optimized parameters for each nucleus, is demonstrated. On the other hand, the 2.19 version of the nuclear reaction code EMPIRE-II has been used for this work due to its advantage of including the PE exciton model for cluster emission [11]. At the same time, besides the adoption of default parameters, the Hybrid Monte-Carlo simulation approach has been selected for the nucleon PE due to our interest in the neutron energies higher than 30 MeV.

3.2 *Local approach*

The particular properties of various target nuclei and reaction channels have been considered by using a consistent local parameter set, established on the basis of various independent data in a small range of mass and charge numbers. A generalized Geometry-Dependent Hybrid (GDH) model [33,34] for PE processes in STAPRE-H version of the original code [35] includes the angular-momentum conservation [36] and the α -particle and deuteron emission based on a pre-formation probability φ [37] with the values in the present work of 0.2 for α -particles and 0.4 for deuterons [2]. The same optical potential and nuclear level density parameters have been used in the framework of the OM [38], GDH and HF models, for calculation of the intra-nuclear transition rates and single-particle level (s.p.l.) densities at the Fermi level [34,39,40], respectively, in the former case.

The nucleon optical potential of Koning and Delaroche [22], used by default in both TALYS and EMPIRE codes, has obviously been the first option. However, a basic point revealed by these authors is that their global potential does not reproduce the minimum around the neutron energy of 1-2 MeV for the total neutron cross sections of the $A\sim 60$ nuclei. Following also their comment on the constant geometry parameters which may be responsible for this aspect, we have applied the SPRT method [41] for determination of the OMP parameters over a wide neutron energy range through analysis of the s - and p -wave neutron strength functions, the potential scattering radius R' and the energy dependence of the total cross section $\sigma_T(E)$. The recent RIPL-2 recommendations [24] for the low-energy neutron scattering properties and the available measured σ_T data (Fig. 1) have been used in this respect, and we found that it is necessary to consider the energy dependence of the real potential geometry at lower energies shown in Table 2. These potentials were used also for the calculation of the collective inelastic scattering cross sections by means of the direct-interaction distorted-wave Born approximation (DWBA) method and a local version of the computer code DWUCK4 [42]. The weak coupling model was adopted in this respect for the odd nuclei ^{55}Mn and $^{63,65}\text{Cu}$ using the collective state parameters of Kalbach [27]. Typical ratios of the direct inelastic scattering to the total reaction cross sections in the energy range from few to 60 MeV decrease from ~ 11 to 5%, for the ^{55}Mn nucleus, and from ~ 8 to 3% for the Cu isotopes.

The OMP of Koning and Delaroche [22] was considered also for the calculation of proton transmission coefficients on the residual nuclei, i.e. the isotopes of Cr and Ni, while a former trial of this potential concerned the proton reaction cross sections σ_R [43]. Since these data are missing for the Cr nuclei, our local analysis involved the isotopes of Mn, Fe, Co, Ni, Cu and Zn, for lower energies important in statistical emission from excited nuclei. The comparison of these data and results of either the local OMP predictions when they are available in Table 8 of Ref. [22] or otherwise their proton global OMP is shown in Fig. 2. A very good agreement exists apart from the isotopes of Fe and in particular Ni, with the data overpredicted by about or higher than 10%. In order to obtain the agreement with the corresponding σ_R data (Fig. 2) we have found necessary to replace the constant real potential diffusivity $a_V=0.663$ fm [22] by the energy-dependent forms $a_V=0.563+0.002E$ up to 50 MeV for the target nucleus ^{56}Fe , and $a_V=0.463+0.01E$ up to 20 MeV for ^{58}Ni , where the energy E is in MeV and the diffusivity in fm. A final validation of both the original OMP and the additional energy-dependent a_V has been obtained by analysis of the available (p, γ) and (p,n) reaction data up to $E_p \sim 12$ MeV on Cr (Fig. 3) and Ni isotopes (Fig. 4) while the other statistical model parameters are the same as in the rest of the present work. It can be seen that these reaction data have been quite well reproduced, with an increase of the related accuracy within 10% provided by the energy dependence adopted for the real potential diffusivity at lower energies.

The optical potential which is used in this work for calculation of the α -particle transmission coefficients was established previously [44] for emitted α -particles, and supported recently by semi-microscopic analysis for $A\sim 90$ nuclei [45]. On the other hand, by comparison of the present calculations and measured data [46] for the target nuclei $^{63,65}\text{Cu}$ we found that the real well diffuseness a_R of the above-mentioned global OMP should be changed to 0.67 fm. This reduction is rather similar to that found necessary for the target nuclei ^{59}Co , and $^{58,60,62}\text{Ni}$ [2], so that it has been taken into account also for ^{55}Mn . Lastly, the calculation of the deuteron transmission coefficients has been carried out by using the global OMP of Lohr and Haeberli [47] and validated throughout analysis of the deuteron-emission spectra at 14.8 MeV [48].

The back-shifted Fermi gas (BSFG) formula has been used for the excitation energies below the neutron-binding energy, with the parameters a and Δ (Table 3) obtained by a fit of the recent experimental low-lying discrete levels [49] and s -wave nucleon resonance spacings D_0 [24]. Actually the same approach basis [50,51,52,53] and similar parameters have been used as previously within this mass range [1,2], updated by means of the new structure data published in the meantime. Concerning the particle-hole state density playing for PE description the same role as the nuclear-level density for statistical model calculations, a composite formula [40] was involved within the GDH model. Thus no s.p.l.-density free parameter except for the α -particle state density [37] $g_\alpha=A/10.36 \text{ MeV}^{-1}$ was used for the PE account.

The modified energy-dependent Breit-Wigner (EDBW) model [55,56] was used for the electric dipole γ -ray strength functions $f_{E1}(E_\gamma)$ of main importance for calculation of the γ -ray transmission coefficients, also as previously within this mass range [1,2]. The corresponding $f_{E1}(E_\gamma)$ values have been checked within the calculations of capture cross sections of Mn and Cu isotopes in the neutron energy range from keV to 3-4 MeV, by using the OMP and nuclear level density parameters described above and global estimations [50] of the γ -ray strength functions for multipoles $\lambda \leq 3$. Thus we found that the $f_{E1}(E_\gamma)$ strength functions corresponding to the experimental [24] average radiative widths $\Gamma_{\gamma_0}^{exp}$ provide an accurate description of the capture data for the Cu isotopes (Fig. 5) while an increased value $\Gamma_{\gamma_0} \sim 1300 \text{ meV}$ has been required in the same respect for the ^{55}Mn nucleus. Finally, the accuracy of the γ -ray strength functions adopted in this work is shown also by the above-mentioned analysis of the (p, γ) reaction cross sections (Figs. 3-4).

4 Activation cross sections

The results of the measurements are summarized in Table 1 and are shown in Figs. 6-8, using the notation of the preliminary data in Refs. [13,14], along

with the model calculations. The comparison with the previous experimental data concerns in general measurements done after the end of '60s. A detailed discussion is firstly given below for the new experimental cross sections in comparison with previous data as well as the actual calculated values.

The $^{55}\text{Mn}(n,2n)^{54}\text{Mn}$ reaction cross section. Eight new experimental values in the present work cover the energy range from 13.56 to 14.78 MeV (Fig. 6). The new data agree within the error limits with the earlier measurements, being however higher than the most recent previous data from the middle of the last decade but systematically lower with respect to the ones measured in the end of 80's. They seem thus to provide a better confined range of these reaction cross sections around 14 MeV, within an accuracy of 3-4% which is most important for the validation of model calculations at a similar level. In spite of the smaller weight of PE processes at these energies, of around 15% of the total reaction cross section, this increased level of accuracy is already acting as a rigorous assessment of the model parameters. The rather similar agreement with these data is a good point for all three calculations, while larger differences come out just above this energy range. The good agreement of the local calculation is mostly due to the local set up of level density parameters by fitting of the recent resonance data and low-lying level schemes.

The $^{55}\text{Mn}(n,\alpha)^{52}\text{V}$ reaction cross section. The nine cross section values measured between 13.47 and 14.83 MeV, together with the more recent data of Fessler et al. [57], settle with enlarged accuracy the maximum of this reaction excitation function. It appears to be lower by $\sim 20\%$ with regard to the data prior 90's, making thus possible an enhanced knowledge of this excitation function. Therefore it results now an obvious change of the slope of data up to the incident energy of 12 MeV [58], which is described only by one global calculation. The difference of the same model prediction with all data above this energy is pointing out the less usual trend of the measurement results at the lower energies. Since, on the other hand, the agreement found for the $^{55}\text{Mn}(n,p)^{55}\text{Cr}$ reaction (Fig. 6) between model calculations and the measured cross sections also by Bostan and Qaim [58] is supporting the assumption of a different reaction process leading to the extra α -particle yield at the corresponding excitation energies in compound nuclei around 12–18 MeV. The enhancement related to the position of a giant quadrupole resonance (GQR) at these energies has also been found and discussed for the (n,α) reaction on $^{92,98}\text{Mo}$ [45].

The $^{63}\text{Cu}(n,\alpha)^{60}\text{Co}$ reaction cross section. There is a similar case for this reaction as the above-mentioned one for the target nucleus ^{55}Mn . The nine cross sections measured also between 13.47 and 14.83 MeV remove the ambiguity of about 20% between various sets of measured cross sections at these energies. Thus, together with the recent measurement of Plompen et al. [46,59], they outline the maximum of this reaction excitation function while the lat-

ter data set completes this excitation function at higher energies (Fig. 7). A previous recent analysis of this reaction [59] by using even earlier versions of TALYS and EMPIRE-II codes has actually resolved the questions existing on its description over the whole energy range. The present global predictions of the two codes are rather similar to the former values [59], as well as to the instance of the above-discussed reaction $^{55}\text{Mn}(n,\alpha)^{52}\text{V}$ while the agreement of our local calculations is significant especially with reference of the simultaneous description of the data for all reaction channels and both stable isotopes of copper.

The $^{65}\text{Cu}(n,2n)^{64}\text{Cu}$ reaction cross section. The data obtained for this reaction are in good agreement with the most recent experimental data. Moreover, they confirm a sudden change of the ascending slope of the excitation function (Fig. 8), which correspond in the GDH model to the opening of the partial wave $l=5$ contribution for the PE mechanism (see the discussion on Fig. 4 of Ref. [3] and below).

The $^{65}\text{Cu}(n,p)^{65}\text{Ni}$ reaction cross section. The eight new cross section values of the present work from 13.56 to 14.78 MeV reduce the spread of the previous measured data from over $\sim 40\%$ (Fig. 8). They are close but slightly lower than the most recent measurements [46] setting up a strong checking point for model calculations. The results of the TALYS code and the local approach agree well with them while the EMPIRE-II predictions are too large. One may consider at this point that all EMPIRE-II calculations in this work made use of the Hybrid Monte-Carlo simulation approach for the PE component description, which is the choice recommended by the authors [11] for neutron energies higher than 30 MeV. It can be seen that the actual TALYS-0.72 and EMPIRE-II predictions are becoming similar above 20–30 MeV (Figs. 6-8).

The present analysis of the fast-neutron reactions on the stable isotopes of Mn and Cu involved calculations for the production of the ground and isomeric states ^{52g}Mn (6^+ , 5.6 d), ^{60m}Co (2^+ , 10.5 min), ^{62g}Co (2^+ , 1.5 min), ^{62m}Co (5^+ , 13.91 min). The production of both low- and high-spin isomers supports the assumptions adopted, e.g. within local-parameter calculations, for the level density angular-momentum distribution as well as the γ -ray strength functions. In the case of α -particle emission channels this work has additionally validated the angular-momentum conservation within the PE model.

5 Outlook of the pre-equilibrium reactions account

The formerly-mentioned needs of sound, complete and reliable neutron-induced cross section data for Mn and Cu also enabled a stringent test of the various nuclear models as well as their corresponding account of particular effects.

However, the key points in this respect are related to the PE description, which becomes increasingly significant at higher energies. Thus, it seems of relevance to look for the answers which may be provided by the data analysis firstly below and then above the incident energy of 20 MeV. Since this is the upper limit of the energy range where neutron data are generally considered to be reasonably well known, the present discussion may also reveal the eventual need for more measurements at higher energies. It has been carried out within the local approach, based on the use of a consistent parameter set already established on the basis of ancillary independent data. On the other hand, the insight of the calculated results, corresponding to distinct parameter values or model assumptions, may contribute to the understanding of the variance shown by the three model calculations in Figs. 6–8. Actually, an ultimate goal of this investigation is to increase the global predictions accuracy to the level of local analysis.

5.1 Calculated cross-section sensitivity to model parameters, below 20 MeV

5.1.1 Sensitivity to optical potential parameters

A first point, following the optical potential analysis described in Section 3.2, should concern the effects of the neutron and proton modified OMPs on the calculated reaction cross sections. The larger amount of data existing for the (n,2n) and (n,p) reactions on ^{65}Cu have been involved in this respect as it is shown in Fig. 9. Thus, firstly one may note that the modified neutron potential (Table 1) is leading to a decrease of $\sim 5\%$ for the (n,2n) reaction calculated cross sections, with respect to the results obtained by using the original OMP [22]. Similarly, the modified proton potential of Koning and Delaroche leads to a decrease of $\sim 20\%$ of the calculated (n,p) reaction cross sections. On the other hand, joining together the two changes in the case of the (n,p) reaction, results in a compensation of the latter one and a reduced final change of $\sim 10\%$ for the calculated cross sections. Therefore, the additional analysis of the nucleon OMP improved the accuracy of the calculated cross sections from $\sim 20\%$, for the smaller cross sections, to around 5% for the major reaction channels. In fact, this better precision is closer to the above-mentioned range of 3-4% accuracy of the new measured cross sections around 14 MeV, together making possible an effective trial of the PE model parameters which are responsible for $\sim 15\%$ of the total reaction cross section at these energies.

It was noted in the previous section that, by comparison of the present calculations and measured data [46] for the target nuclei $^{63,65}\text{Cu}$, it was found that the real well diffuseness a_R of the global OMP [44] for emitted α -particles should be decreased to 0.67 fm. Since this reduction is rather similar to that found recently to be needed for the target nuclei ^{59}Co and $^{58,60,62}\text{Ni}$ [2], it has

been taken into account also for the target nucleus ^{55}Mn . However there are a couple of key points related to this matter. First, by using just the global OMP [44] for emitted α -particles, one would obtain also within the local approach calculated cross sections for the reaction $^{55}\text{Mn}(n,\alpha)^{52}\text{V}$ closed to the results provided by the code EMPIRE-II and in very good agreement with the measured cross sections also by Bostan and Qaim [58]. On the other hand, there is no way to explain the rest of corresponding data above the incident energy of 12 MeV, by pure statistical including PE emission.

Second, Yamamuro [60] pointed out, with respect to the clear difference of the α -particle OMPs which are needed for calculation of the (α,n) and (n,α) reaction cross sections, that it is found for closed shell nuclei but not for odd target nuclei such as ^{53}Cr , ^{57}Fe , ^{61}Ni , and ^{67}Zn . However, the present case of the $^{63,65}\text{Cu}$ nuclei comes in addition of those mentioned in Ref. [2], at variance with Yamamuro's statement. Alternatively one may consider the possible enhancement related to the position of a giant quadrupole resonance (GQR) at the excitation energies concerned in these nuclei. Although generally the decay of the GQR is observed with nucleon emission, recent work shows [61] that an appreciable (non-statistical) decay through α -particle emission can occur. An extra yield which could be understood as decay from giant resonances populated via neutron capture has been found as well for the Mo isotopes [45]. Thus it follows that further analysis is required, making use also of microscopic DF potentials based on temperature-dependent nuclear density distributions for the description of (n,α) excitation functions [45].

5.1.2 *Charged-particle emission spectra sensitivity*

Actually one may note the same level of 5–20% differences between the global predictions and the measured cross sections, around the incident energy of 14 MeV, as the OMP has an effect on the calculated cross sections at these energies. Larger divergence occurs at higher energies, where it could be related to the continuously growing importance of PE assumptions and key quantities. However, just the assessment within this energy range of the consistent parameter set involved in the local approach allows for a further focus on differences between the measured and calculated cross sections especially above 20 MeV, in order to establish the correctness of the adopted PE formalism.

Moreover, in spite of the well-known reduced usefulness of 14 MeV neutron reaction data to validate PE calculations for medium-mass nuclei [33], the suitable description of related charged-particle emission spectra may have a twofold outcome. The lowest-energy region of spectra, corresponding to a second emitted particle from a fully equilibrated compound nucleus, may truly validate the OMP used for emitted particles as well as the level density parameters of the excited nuclei. On the other hand, the emission of high-energy

charged particles is entirely due to the PE processes. Thus, advanced pairing and shell corrections of particle-hole state densities could be eventually confirmed by the PE model account of this emission-spectrum energy region.

Comparison of measured angle-integrated proton and α -particle emission spectra from 9 [46,62], 14.1 [63,64] and 14.8 MeV [48] neutron-induced reactions on ^{55}Mn and $^{63,65}\text{Cu}$ nuclei and calculated values within the local approach is shown in Fig. 10. The two goals mentioned above can be considered as being satisfied, with a couple of additional comments. While the measured particle spectra of Ref. [48] are given in the laboratory system, their conversion to the center-of-mass system is equivalent to a shift of the spectrum to higher energies, of up to one MeV for the most energetic α -particles (see, e.g., Refs. [65,66]). Thus a good agreement is seen between the measured and calculated α -particle emission spectra for $^{63,65}\text{Cu}$ nuclei, apart from considerably higher measured data for the high energy parts of the spectra corresponding to excitations below ~ 2 MeV in the residual nuclei $^{60,62}\text{Co}$. The same effect is seen in the case of the target nucleus ^{55}Mn , for which the experimental α -particle spectra [63,64] are given as function of channel energy and no further conversion is necessary for comparison with the model calculation. This underestimation was noted as well for other target nuclei in this mass region [65,66], indicating that there may be considerable direct excitation of residual nuclei low lying levels beyond the validity of the PE models.

Concerning the additional underestimation of the α -particle spectrum on ^{55}Mn at lowest energies, one should note that the measurements are complicated in this energy range by a rather large background [66].

5.2 *Model-analysis support above 20 MeV*

Above the neutron incident energy of 20 MeV, particularly at excitation energies beyond 30 MeV, the PE model becomes increasingly important in determining the reaction cross section. The lack of free parameters within the corresponding GDH model, as well as the consistent use of the same optical potential and nuclear level density parameters as the HF model, make possible a focus on the correctness of the main related quantity which is the particle-hole state density.

5.2.1 *Nuclear potential finite-depth correction*

The original GDH formalism [33,34] considered a Fermi distribution for the nuclear matter density, with the Fermi energy $F=40$ MeV at saturation density. On this basis it takes into account the nuclear surface effects by means, firstly, of the sum of contributions due to different entrance channel partial

waves l for the first projectile-target interaction. The relevant parameters in this case are averaged over the nuclear densities corresponding to the entrance-channel trajectories from a point at which the nuclear density is $\sim 1/150$ of its saturation value to the radius $R_l = \lambda(l + \frac{1}{2})$. Secondly, lower local-density Fermi energies [67] calculated for each of these trajectories, $F_1(R_l)$, have been considered within the particle-hole state densities (PSD) and limited the hole degrees of freedom. They correspond to a finite well depth correction which has been included [28] in the PSD equidistant spacing model at the same time as the advanced pairing [68] and shell corrections [69] added to the Pauli correction, and the non-equidistant single-particle levels [70]. All of the above were included in a PSD composite formula [40] added to the GDH model within the STAPRE-H code, and were part of previous studies carried out in a similar way [1,2,3,4] but at incident energies up to 20 MeV. The extension of the present analysis to 40 MeV, by means of the measured data put together in Figs. 11-12, is able to check the importance of the finite-depth correction in the frame of the PSD composite formula [40].

Thus, the vanishing of this correction is obtained by replacing the local-density Fermi energies $F_1(R_l)$ with the Fermi energy central value $F=40$ MeV. The results of this exercise are shown in Fig. 11, the most apparent and direct view corresponding to the $^{65}\text{Cu}(n,p)^{65}\text{Ni}$ reaction. The GDH l -dependent finite-depth corrections $F_1(R_l)$ allow the opening only with the energy increase of the PE contribution due to each higher partial wave. This attribute, together with the decreasing total reaction cross section σ_R with energy increasing, leads to a rising fraction σ_{PE}/σ_R but a rather constant (n,p) reaction cross section above the incident energy ~ 20 MeV where the emission of a second neutron becomes possible. By raising the local-density Fermi energies to the central value, the PE contributions of all partial waves become possible from the beginning, in the limit set by the corresponding transmission coefficients. Thus the fraction σ_{PE}/σ_R will increase faster while, e.g., the (n,p) reaction cross section will decrease continuously after getting a higher maximum. The latter two attributes are both opposed to the experimental data, even if their energy dependence above 20 MeV is only fairly accurate. The same findings follow the analysis of the other data above 20 MeV shown in Fig. 11, as well as the reaction $^{65}\text{Cu}(n,2n)^{64}\text{Cu}$ added for completion. Changes of the calculated reaction cross sections above the incident energy of 20 MeV, corresponding to this finite-depth correction, are going from $\sim 50\%$ to more than 100%. A similar result was noticed by Korovin et al. [71], within a modified GDH model and using the former PSD formula of Ericson, while the present results are based on the composite formula [40]. However, excepting the (n,4n) and (n, α) reactions on ^{55}Mn and the (n,3n) reaction on ^{63}Cu , the need for more accurate measured data at least up to 40 MeV is obvious.

5.2.2 Single-particle levels density effects

The Fermi-gas model (FGM) energy dependence of the s.p.l. density has been used within the PSD composite formula [40], in the present local approach as well as in the recent similar analyses [1,2,3,4], following the study and conclusions of Herman et al. [70]. Actually average values of the s.p.l. of excited particles and holes, $g_p(p, h)=g(F + \bar{u}_p)$ and $g_p(p, h)=g(F - \bar{u}_h)$ respectively, have been obtained corresponding to the average excitation energies for particles and holes \bar{u}_p and \bar{u}_h [40]. The s.p.l. density value at the Fermi level has been derived on the basis of its relation to the nuclear level density parameter, $g(F)=\frac{6}{\pi^2}a$, by using the parameter values given in Table 3. By replacing the above-mentioned average energy-dependent s.p.l. $g_{p(h)}(p, h)$ with the constant value $g(F)$ result in the changes shown in Fig. 11. They are quite small below 20 MeV, increasing for the incident energies up to 40 MeV from $\sim 5\%$ to 20%.

Two features should be pointed out at this time. Firstly, the energy dependence of the s.p.l. density is much less important than its value at the Fermi energy [4]. This is a consequence of the fact that the PE cross section is determined by a ratio of the particle-hole level densities corresponding to exciton configurations which differ by one excited particle [33,34,39]. Secondly, this change may become significant at energies higher than 40 MeV.

5.2.3 Nuclear-shell effects

The PSD composite formula [40] included the advanced pairing [68] and shell corrections [69] added to the Pauli correction, by taking into account the nuclear-shell effects through an additional back-shift S of the effective excitation energy [69]. It has been connected, for the excitation energies lower than the binding energy, to the BSFG virtual ground-state shift parameter $\Delta=U_p+S$, where the former term is a constant pairing correction corresponding to the PSD closed formula [69]. The washing out of shell effects above the neutron binding was taken into account also for the back-shift S value by using the shell correction within the approach of Junghans et al. [52], derived as mentioned in Section 3.2.3, with a similar smooth transition between the two energy range as for the nuclear level density. Obviously, the largest effect of this PSD correction corresponds to the lowest excitation energies, the related S -values causing up the high-energy limit of the emitted-particle spectra (e.g., Fig. 10). Since the shift Δ is around and less than zero value for the odd- A and odd-odd nuclei, respectively, the back-shift S is negative for most of the nuclei involved in the present work. It leads to enlarged effective excitation energies for the PSD calculation at lower excitations, finally increasing the PE cross sections. In Fig. 11 is also shown the effect of removing the shell correction in the PSD composite formula, the subsequent decrease of the PE component leading to, e.g., (n,2n) and (n,3n) reaction cross sections decreased

by 5–10% around the maximum of their excitation functions but (n,p) reaction cross sections which decrease by $\sim 20\%$, around the incident energy of 14 MeV, up to more than 50% at 40 MeV. The effect is obviously less important for (n,4n) reactions, at least at the energies involved in this work, where multiple PE processes are not important [8]. Nevertheless, consideration of the nuclear-shell effects proves to be quite important within the present analysis, in addition to the influence of the $f_{7/2}$ neutron and proton shell closures on the particle PE spectra [7] already noted.

5.2.4 The s.p.l.-density 'continuum effect'

The 'continuum effect' (CE), i.e. the s.p.l. density decreasing with energy in the continuum region [72,73,74], can be described basically using the corrected s.p.l. density formula [40]

$$g_p(p, h) = g(F) \left[\left(1 + \frac{\bar{u}_p}{F} \right)^{1/2} - \left(\frac{\bar{u}_p - B}{F} \right)^{1/2} \theta(\bar{u}_p - B) \right], \quad (1)$$

where B is the nucleon binding energy. However, for the present reaction cross section calculation, one should also take into account the Coulomb and centrifugal barriers (e.g., [38]). On the other hand, one should note that the role of this effect will be major in the case of the particle-hole configurations of the composite nucleus, excited at higher energies with respect to the residual nuclei.

The progressive addition of these barriers to the binding energy B , as well as the removal of the continuum effect within the PSD calculation, are shown in Fig. 12. The most apparent and direct view can be seen once more in the reaction $^{65}\text{Cu}(n,p)^{65}\text{Ni}$. The decrease of the s.p.l. densities due to the consideration of binding energy alone, with respect to no CE presumed, leads to the increase of PE cross sections. The addition of the Coulomb barrier actually decreases the CE weight, which remains visible only above the incident energy of ~ 25 MeV. Finally, the inclusion also of the centrifugal barrier reduces even more the CE size within the energy range discussed in the present work. The CE complete treatment may again play an important role at higher energies, the steps of its partial account in this analysis being able to shed some light on the expected consequences at these energies.

6 Summary and conclusions

New measurements with the activation technique were performed for neutron-induced reactions around 14 MeV on the stable isotopes of Mn and Cu.

A significant body of experimental data with an accuracy within 3–4% has been obtained by measurements on natural samples for the $^{55}\text{Mn}(n,2n)^{54}\text{Mn}$, $^{55}\text{Mn}(n,\alpha)^{52}\text{V}$, $^{63}\text{Cu}(n,\alpha)^{60}\text{Co}$, $^{65}\text{Cu}(n,2n)^{64}\text{Cu}$, and $^{65}\text{Cu}(n,p)^{65}\text{Ni}$ reactions from 13.47 to 14.83 MeV. The experimental cross sections are compared with the results of calculations for all activation channels for ^{55}Mn and $^{63,65}\text{Cu}$ isotopes, and neutron incident energies below 20 MeV as well as up to 40–50 MeV. The increased accuracy of the present cross sections around 14 MeV has made possible an effective trial of the PE model parameters at the same level, even if this reaction mechanism is responsible at these energies for only $\sim 15\%$ of the total reaction cross section. It should be also noted that similar differences of 5–20% exist between the global predictions and the measured cross sections, in the same energy range, as the OMP effects on the calculated cross sections. On the other hand, this assessment of the consistent parameter set involved in the local analysis below 20 MeV allows a further focus at higher energies on differences between the measured and calculated cross sections related to model assumptions. The few more recent data of increased accuracy between ~ 14 and 20–21 MeV are also quite useful in this respect.

Larger divergence between the measured and calculated cross sections occurs mainly for the global predictions at higher energies, where the importance of PE assumptions and key quantities is continuously increasing. Since an ultimate goal of this investigation is to increase the global prediction accuracy to the level of local analysis, we have looked for the significant effects related to distinct parameter or model assumptions. The most important is found to correspond within the GDH model to the nuclear potential finite-depth correction taken into account for description of particle-hole state densities. Its omission leads to a large increase of the PE weight as well as to reaction cross section changes going from $\sim 50\%$ to more than 100%. However, the need for more accurate measured data at least up to the incident energy of 40 MeV is obvious. A similar case is shown by consideration of the nuclear-shell effects within the PSD formula. On the other hand, there are effects such as the s.p.l.–density energy dependence and inclusion of the '*continuum effect*' which may however become significant at energies higher than 40 MeV. Therefore, the present discussion is also pointing out the usefulness of further measurements of neutron activation reactions at higher incident energies below, e.g., 40 MeV [75] as well as up to 100 MeV [76].

Acknowledgments

Work supported in part by the European Community EFDA under the Contract of Association EURATOM–MEdC (Bucharest), and MEdC Contract No. CEEEX-05-D10-48 .

References

- [1] P. Reimer, V. Avrigeanu, A.J.M. Plompen, S.M. Qaim, Phys. Rev. C 65 (2001) 014604.
- [2] V. Semkova, V. Avrigeanu, T. Glodariu, A.J. Koning, A.J.M. Plompen, D.L. Smith, S. Sudar, Nucl. Phys. A 730 (2004) 255.
- [3] P. Reimer, V. Avrigeanu, S. Chuvaev, A.A. Filatenkov, T. Glodariu, A.J. Koning, A.J.M. Plompen, S.M. Qaim, D.L. Smith, H. Weigmann, Phys. Rev. C 71 (2005) 044617.
- [4] V. Avrigeanu, R. Eichin, R.A. Forrest, H. Freiesleben, M. Herman, A.J. Koning, K. Seidel, Nucl. Phys. A 765 (2006) 1.
- [5] R.A. Forrest, J. Kopecky, Fus. Eng. Design 82 (2007) 73.
- [6] R.A. Forrest, J. Kopecky, J.-Ch Sublet, Report UKAEA FUS 535, UKAEA Culham Science Centre, March 2007.
- [7] M. Blann, S.M. Grimes, L.F. Hansen, T.T. Komoto, B.A. Pohl, W. Scobel, M. Trabandt, C. Wong, Phys. Rev. C 28 (1983) 1475.
- [8] A.J. Koning, M.C. Duijvestijn, Nucl. Phys. A 744 (2004) 15.
- [9] S.J. Mills, G.F. Steyn, F.M. Nortier, in *Proc. Int. Conf. on Nuclear Data for Science and Technology, Jülich, May 1991*, edited by S.M. Qaim (Springer-Verlag, Berlin, 1992), p. 708.
- [10] A.J. Koning, S. Hilaire, M.C. Duijvestijn, in: R.C. Haight, M.B. Chadwick, T. Kawano and P. Talou (Eds.), *Proc. Int. Conf. on Nuclear Data for Science and Technology, 2004, Santa Fe, AIP Conf. Proc. No. 769* (American Institute of Physics, New York, 2005), p. 1154; www.talys.eu .
- [11] M. Herman, P. Oblozinsky, R. Capote, M. Sin, A. Trkov, A. Ventura, V. Zerkin, in: R.C. Haight, M.B. Chadwick, T. Kawano and P. Talou (Eds.), *Proc. Int. Conf. on Nuclear Data for Science and Technology, 2004, Santa Fe, AIP Conf. Proc. No. 769* (American Institute of Physics, New York, 2005), p. 1184; EMPIRE-II v.2.19, <http://www-nds.iaea.org/empire/> .
- [12] M. Avrigeanu, V. Avrigeanu, STAPRE-H95 Computer Code, IPNE Report NP-86-1995, Bucharest, 1995 and references therein; News NEA Data Bank 17 (1995) 22.
- [13] A.A. Filatenkov, S.V. Chuvaev, V.G. Khlopin Radium Institute Report RI-252 (in Russian), CNIIatominform, Moscow, 1999.
- [14] A.A. Filatenkov, S.V. Chuvaev, Khlopin Radium Institute Preprint KRI-259 (in Russian), CNIIatominform, Moscow, 2003.
- [15] A.A. Filatenkov, S.V. Chuvaev, V.G. Khlopin Radium Institute Report KRI-258 (2001).

- [16] M. Drosig, Report IAEA-NDS-87, IAEA, Vienna, 2000 (unpublished), www-nds.iaea.org/drosg2000.html .
- [17] H.H. Anderson, J.F. Ziegler, Hydrogen Stopping Powers and Ranges in All Elements (Pergamon, New York, 1977).
- [18] A.A. Filatenkov, S.V. Chuvaev, V.A. Jakovlev, and V.P. Popik, Fusion Eng. and Design 37 (1997) 151; A.A. Filatenkov, S.V. Chuvaev, V.N. Aksenov, V.A. Jakovlev, International Atomic Energy Agency (IAEA) Report INDC(CCP)-402, Vienna, 1997.
- [19] A.B. Pashchenko, H. Wienke, J. Kopecky, J-Ch. Sublet, R.A. Forrest, Report IAEA-NDS-173 (1997).
- [20] M. Wagner, H. Vonach, A. Pavlik, B. Strohmaier, S. Tagesen, J. Martinez-Rico, Physics Data 13-5, 1990.
- [21] R.B. Firestone, Table of Isotopes, 8th Ed. (Wiley, New York, 1995).
- [22] A.J. Koning, J.P. Delaroche, Nucl. Phys. A 713 (2003) 231.
- [23] J. Raynal, Tech. Rep. CEA-N-2772, CEA, Saclay, 1994.
- [24] IAEA-CRP Reference Input Parameter Library (RIPL-2), <http://www-nds.iaea.or.at> .
- [25] A.V. Ignatyuk, G.N. Smirenkin, A.S. Tishin, Yad. Fiz. 21 (1975) 485; Sov. J. Nucl. Phys. 21 (1976) 255.
- [26] C. Kalbach, Phys. Rev. C 33 (1986) 818.
- [27] C. Kalbach, Phys. Rev. C 62 (2000) 44608.
- [28] C. Kalbach, Phys. Rev. C 32 (1985) 1157.
- [29] A.J. Koning, M.C. Duijvestijn, Nucl. Instr. Meth. B248 (2006) 197.
- [30] M.C. Duijvestijn, A.J. Koning, Ann. Nuc. En. 33 (2006) 1196.
- [31] A.J. Koning, M.C. Duijvestijn, S.C. van der Marck, R. Klein Meulekamp, A. Hogenbirk, accepted for publication in Nucl. Sci. Eng. (2007).
- [32] A.J. Koning and M.C. Duijvestijn, accepted for publication in Journ. Nucl. Sci. Techn. (2007).
- [33] M. Blann, H.K. Vonach, Phys. Rev. C 28 (1983) 1475.
- [34] M. Blann, Nucl. Phys. A 213 (1973) 570.
- [35] M. Uhl, B. Strohmaier, Report IRK-76/01, IRK, Vienna, 1981.
- [36] M. Avrigeanu, M. Ivascu, V. Avrigeanu, Z. Phys. A 329 (1988) 177; 335 (1990) 299.
- [37] E. Gadioli, E. Gadioli-Erba, Z. Phys. A 299 (1981) 1.

- [38] O. Bersillon, Centre d'Etudes de Bruyeres-le-Chatel, Note CEA-N-2227, 1981.
- [39] M. Avrigeanu, V. Avrigeanu, J. Phys. G: Nucl. Part. Phys. 20 (1994) 613.
- [40] M. Avrigeanu, V. Avrigeanu, Comp. Phys. Comm. 112 (1998) 191; A.Harangozo, I.Stetcu, M.Avrigeanu, V.Avrigeanu, Phys. Rev. C 58 (1998) 295.
- [41] J.P. Delaroche, Ch. Lagrange, J. Salvy, IAEA-190 (IAEA, Vienna, 1976), vol. 1, p. 251.
- [42] P.D. Kunz, DWUCK4 user manual, OECD/NEA Data Bank, Issy-les-Moulineaux, France, 1984; www.nea.fr/abs/html/nesc9872.html
- [43] R.F. Carlson, At. Data Nucl. Data Tables 63 (1996) 93.
- [44] V. Avrigeanu, P.E. Hodgson, M. Avrigeanu, Phys. Rev. C 49 (1994) 2137.
- [45] M. Avrigeanu, W. von Oertzen, V. Avrigeanu, Nucl. Phys. A 764 (2006) 246.
- [46] EXFOR Nuclear Reaction Data, <http://www-nds.iaea.or.at/exfor> , <http://www.nndc.bnl.gov/nndc/exfor> .
- [47] J.M. Lohr, W. Haeberli, Nucl. Phys. A 232 (1974) 381.
- [48] S.M. Grimes, R.C. Haight, K.R. Alvar, H.H. Barschall, R.R. Borchers, Phys. Rev. C 19 (1979) 2127.
- [49] Evaluated Nuclear Structure Data File (ENSDF), <http://www.nndc.bnl.gov/ensdf/index.jsp> .
- [50] C.H. Johnson, Phys. Rev. C 16 (1977) 2238.
- [51] V. Avrigeanu, T. Glodariu, A.J.M. Plompen, H. Weigmann, J. Nucl. Sci. Tech. Suppl. 2 (2002) 746.
- [52] A.R. Junghans, M. de Jong, H.-G. Clerc, A.V. Ignatyuk, G.A. Kudyaev, K.-H. Schmidt, Nucl. Phys. A 629 (1998) 635.
- [53] A.J. Koning, M.B. Chadwick, Phys. Rev. C 56 (1997) 970.
- [54] H. Vonach, M. Uhl, B. Strohmaier, B.W. Smith, E.G. Bilpuch, G.E. Mitchell, Phys. Rev. C **38**, 2541 (1988).
- [55] D.G. Gardner, F.S. Dietrich, Report UCRL-82998, LLNL-Livermore, 1979.
- [56] M. Avrigeanu, V. Avrigeanu, G. Cata, M. Ivascu, Rev. Roum. Phys. 32 (1987) 837.
- [57] A. Fessler, A.J.M. Plompen, D.L. Smith, J.W. Meadows, Y. Ikeda, Nucl. Sci. Eng. 134 (2000) 171.
- [58] M. Bostan, S.M. Qaim, Phys. Rev. C 49 (1994) 266.
- [59] V. Semkova, A.J.M. Plompen, D.L. Smith, as Ref. [11], p. 1019.
- [60] N. Yamamuro, Nucl. Sci. Eng. 122 (1996) 374.

- [61] M. Fallot, J.A. Scarpaci, N. Frascaria, Y. Blumenfeld, A. Chbihi, Ph. Chomaz, P. Desesquelles, J. Frankland, E. Khan, J.L. Laville, E. Plagnol, E.C. Pollacco, P. Roussel-Chomaz, J.C. Roynette, A. Shrivastava, T. Zerguerras, Phys. Lett. B 613 (2005) 128.
- [62] C. Tsabaris, E. Wattecamps, G. Rollin, C. Papadopoulos, Nucl. Sci. Eng. 128 (1998) 47.
- [63] R. Fischer, G. Traxler, H. Vonach, M. Uhl, Rad. Effects 96 (1986) 309.
- [64] R. Fischer, G. Traxler, M. Uhl, H. Vonach, Phys. Rev. C 34 (1986) 460.
- [65] C. Derndorfer, R. Fischer, P. Hille, H. Vonach, P. Maier-Komor, Z. Phys. A 301 (1981) 327.
- [66] R. Fischer, G. Traxler, M. Uhl, H. Vonach, Phys. Rev. C 30 (1984) 72.
- [67] E. Gadioli, E. Gadioli Erba, P.G. Sona, Nucl. Phys. A 217 (1973) 589.
- [68] C. Kalbach, Nucl. Sci. Eng. 95 (1987) 70; Z. Phys. A 332 (1989) 397.
- [69] C.Y. Fu, Nucl. Sci. Eng. 86 (1984) 344.
- [70] M. Herman, G. Reffo, R. Rosetti, G. Giardina, A. Italiano, Phys. Rev. C 40 (1989) 2870.
- [71] Yu.A. Korovin, A.Yu. Konobeyev, P.E. Pereslavl'tsev, A.Yu. Stankovsky, C. Broeders, I. Broeders, U. Fischer, U. von Möllendorff, Nucl. Instr. Meth. A 463 (2001) 544.
- [72] S. Shlomo, Nucl. Phys. A 539 (1992) 17.
- [73] Ye.A. Bogila, V.M. Kolomietz, A.I. Sanzhur, S. Shlomo, Phys. Rev. C 53 (1996) 855.
- [74] S. Shlomo, V.M. Kolomietz, H. Dejbakhsh, Phys. Rev. C 55 (1997) 1972.
- [75] X. Ledoux, S. Simakov, in *The SPIRAL2 Project. Neutrons For Science* (GANIL, Caen, 2006), <http://www.ganil.fr/research/developments/spiral2/> .
- [76] A. Mengoni, F. Kppeler, E. Gonzales Romero et al. (The n_TOF Collaboration), *n_TOF-Ph2 Activities at the neutron time of flight facility at CERN* (CERN, Geneva, 2005), http://www.cern.ch/ntof/Documents/LoI_2005/ .

Figure captions

FIG. 1. Comparison of experimental and calculated neutron total cross sections for ^{55}Mn and $^{63,65,\text{nat}}\text{Cu}$ target nuclei, by using the global (dotted curves) and local (dashed curves) OMP parameter sets of Koning and Delaroche [22], and the changes of the latter given in Table 1 (solid curves). The experimental data are taken from the EXFOR database [46].

FIG. 2. Comparison of the measured [43] and calculated proton reaction cross sections on all stable isotopes of Mn, Fe, Co, Ni, Cu and Zn, by using either the local OMP predictions of Koning and Delaroche when they are available in Table 8 of Ref. [22] or otherwise their proton global OMP (dotted, dash-dotted and dashed curves) and the modified parameter set mentioned in the text for the target nuclei ^{56}Fe and ^{58}Ni (solid curves).

FIG. 3. Comparison of the measured [46] and calculated proton reaction cross sections (dash-dotted curve), (p, γ) and (p,n) reaction cross sections up to $E_p \sim 12$ MeV on Cr isotopes by using the OMP parameter sets mentioned for Fig. 2.

FIG. 4. As for Fig. 3, but for the Ni isotopes.

FIG. 5. Comparison of the measured [46] neutron-capture cross sections of ^{55}Mn and $^{63,65,\text{nat}}\text{Cu}$ target nuclei, for incident energies up to 3–4 MeV, and calculated values by using the computer codes TALYS-0.72 (dashed curves) and EMPIRE-II (dash-dotted curves) with default global parameters, and the local analysis with γ -ray strength functions $f_{E1}(E_\gamma)$ within the EDBW model corresponding to either the experimental [24] average s -wave radiative widths $\Gamma_{\gamma 0}$ (dotted curves), or $\Gamma_{\gamma 0}$ values corresponding to a fit of experimental neutron capture data (solid curves).

FIG. 6. Comparison of measured [46] and calculated neutron-activation cross sections for the target nucleus ^{55}Mn , by using the computer codes TALYS-0.72 (dashed curves) and EMPIRE-II (dash-dotted curves) with default global parameters, and STAPRE-H (solid curves) with the local parameter set given in this work.

FIG. 7. As for Fig. 6, but for the target nucleus ^{63}Cu .

FIG. 8. As for Fig. 6, but for the target nucleus ^{65}Cu .

FIG. 9. Comparison of measured [46] and calculated cross sections within the local approach for the (n,2n) and (n,p) reactions on the target nucleus ^{65}Cu , by using the OMP parameter sets of Koning and Delaroche [22] (dotted curves), and corresponding changes for the proton OMP (dashed curve) and neutron

OMP (solid curves).

FIG. 10. Comparison of measured [46,48,62,63,64] angle-integrated proton and α -particle emission spectra from 9, 14.1 and 14.8 MeV neutron-induced reactions on the ^{55}Mn and $^{63,65}\text{Cu}$ nuclei and calculated values within the local approach for the PE emission (dashed curves), statistical first- (dash-dotted curves) and second-emitted particles (dotted curves) from equilibrated compound nuclei, and their sum (solid curves).

FIG. 11. Comparison of measured [46] neutron-activation cross sections for the target nuclei ^{55}Mn and $^{63,65}\text{Cu}$ up to 40 MeV, and calculated values with the local parameter set given in this work (solid curves) except for replacement of either the local-density Fermi energies $F_1(R_l)$ with the Fermi energy central value F (dash-dotted curves), or the average energy-dependent s.p.l. densities with the constant value $g(F)$ (dotted curves), as well as for removal of the shell correction S in the PSD composite formula (dashed curves).

FIG. 12. As for Fig. 11, but for removal of the '*continuum effect*' (CE) of the s.p.l. density within the particle-hole state density calculation (dotted curves), and taking into account for this effect the nucleon binding energy B either alone (dash-dotted curves) or together with the Coulomb barrier B_C (dashed curves), while the solid curves correspond to consideration of also the centrifugal barrier B_{CF} .

Table 1

Measured reaction cross sections (mb) for ^{55}Mn and $^{63,65}\text{Cu}$ isotopes between 13.5 and 14.8 MeV. Mean and full widths at half maximum (fwhm) of the neutron energy distribution are shown. The uncertainty of the mean energy is 10 keV. Standard uncertainties are given for the cross sections.

Energy (MeV)	Reaction				
	$^{55}\text{Mn}(n,2n)^{54}\text{Mn}$	$^{55}\text{Mn}(n,\alpha)^{52}\text{V}$	$^{63}\text{Cu}(n,\alpha)^{60}\text{Co}$	$^{65}\text{Cu}(n,2n)^{64}\text{Cu}$	$^{65}\text{Cu}(n,p)^{65}\text{Ni}$
13.47		20.6(8)	47.5(27)		
13.56	620(26)			834(49)	22.33(76)
13.65		20.9(9)	45.6(16)		
13.74	632(26)			863(37)	20.28(127)
13.88		22.6(10)	45.6(25)		
13.96	656(27)			918(62)	21.45(91)
14.05		22.7(10)	45.5(14)		
14.10	690(25)	22.2(10)	45.3(8)	888(25)	21.3(7)
14.19	708(27)			867(37)	20.45(116)
14.27		22.9(10)	45.8(14)		
14.42	740(28)			952(43)	20.36(71)
14.44		23.3(9)	46.1(17)		
14.61	763(27)			903(38)	21.46(65)
14.63		23.5(9)	43.2(15)		
14.78	781(28)			965(50)	20.58(87)
14.83		22.8(10)	42.3(13)		

Table 2

Comparison of experimental [24] and calculated neutron scattering parameters of ^{55}Mn and $^{63,65}\text{Cu}$ isotopes at the neutron energies of 100, 80 and 50 keV, respectively, and (bottom) the changes of OMP parameters [22] which provide the best SPRT results, where the energies are in MeV and geometry parameters in fm.

\ Target	^{55}Mn			^{63}Cu			^{65}Cu		
	S_0*10^4	S_1*10^4	R'	S_0*10^4	S_1*10^4	R'	S_0*10^4	S_1*10^4	R'
Exp.	4.4(6)	0.3(1)		2.1(3)	0.44(7)		2.2(3)	0.47(8)	
Ref. [22] - global	3.8	0.70	6.2	2.2	0.81	7.0	2.1	0.81	7.4
Ref. [22] - local	4.1	0.58	6.2	2.1	0.77	7.1	1.76	0.75	7.4
Ref. [22] - local +	3.8	0.48	4.6	2.2	0.48	6.0	1.92	0.48	6.8
changes:				$r_V=1.260-0.02E, E<3$			$r_V=1.251-0.016E, E<3$		
	$a_V=0.563+0.02E, E<5$			$a_V=0.213+0.15E, E<3$			$a_V=0.303+0.12E, E<3$		

Table 3: The low-lying levels number N_d up to excitation energy E_d [49] used in Hauser-Feshbach calculations, and the low-lying levels and s -wave nucleon-resonance spacings D_0^{exp} (Ref. [24] except otherwise noted) in the nucleon energy range ΔE above the respective binding energy B , for the target-nucleus ground-state spin I_0 , fitted in order to obtain the BSFG level-density parameter a and ground-state shift Δ (corresponding to a spin cut-off factor calculated with a variable moment of inertia between the half and 75% of the rigid-body value, for the excitation energies from g.s. to the nucleon binding energy, and the reduced radius $r_0=1.25$ fm).

Nucleus	N_d	E_d (MeV)	Fitted level and resonance data					a (MeV ⁻¹)	Δ (MeV)
			N_d	E_d (MeV)	$B + \frac{\Delta E}{2}$ (MeV)	I_0	D_0^{exp} (keV)		
⁵⁰ Ti	19	4.940	19	4.94	11.059	7/2	4.0(8)	5.55	1.20
⁵¹ Ti	22	4.187	18	3.77	6.565	0	125(70)	6.05	0.40
⁴⁷ V	23	2.810	23	2.81	7.750	0	36.0(48) ^a	5.50	-1.15
⁴⁸ V	23	1.781	23	1.78				5.95	-1.85
⁴⁹ V	25	2.408	25	2.41	9.559	0	10.6(10) ^a	5.35	-1.80
⁵⁰ V	32	2.162	46	2.65	7.361	7/2	4.1(6)	5.95	-1.75
⁵¹ V	37	3.683	54	4.12	10.646	0	7.9(6) ^a	5.65	-0.68
					11.071	6	2.3(6)		
⁵² V	20	1.843	20	1.84	7.361	7/2	4.1(6)	6.15	-1.60
⁵³ V	25	2.967	25	2.97				5.65	-1.03
⁵⁴ V	19	1.752	17	1.54				5.95	-1.85
⁵⁰ Cr	32	4.363	32	4.36				5.40	0.00
⁵¹ Cr	41	3.448	85	4.29	9.561	0	13.3(13) ^a	5.50	-1.20
⁵² Cr	17	4.100	17	4.10				5.55	0.20
⁵³ Cr	31	3.617	27	3.44	8.432	0	43.40(437)	5.35	-0.90
⁵⁴ Cr	33	4.458	33	4.46	9.817	3/2	7.8(8)	5.55	0.10
⁵⁵ Cr	24	2.895	24	2.90	6.696	0	54.4(8) ^a	6.02	-0.82
							62.0(8)		
⁵⁰ Mn	6	1.143	6	1.14				5.85	-1.40

Table 3: continued.

Nucleus	N_d	E_d (MeV)	Fitted level and resonance data				a (MeV ⁻¹)	Δ (MeV)
			N_d	E_d (MeV)	$B + \frac{\Delta E}{2}$ (MeV)	I_0		
⁵¹ Mn	20	2.984	28	3.29			5.55	-0.85
⁵² Mn	20	2.337	17	2.13			6.00	-1.20
⁵³ Mn	36	3.555	42	3.73			5.35	-1.10
⁵⁴ Mn	24	1.925	24	1.93			6.05	-1.81
⁵⁵ Mn	32	2.953	45	3.07	10.497	0	7.1(7) ^a	-1.55
⁵⁶ Mn	23	1.384	37	1.88	7.374	5/2	2.3(4)	-2.30
⁵⁷ Mn	21	2.233	21	2.33			6.20	-1.25
⁵⁸ Mn	11	0.882	11	0.88			6.65	-1.95
⁵⁸ Fe	42	4.350	60	4.72	10.139	1/2	6.5(10)	0.15
⁵⁹ Fe	28	2.856	28	2.86	6.755	0	25.4(49)	-0.70
⁶⁰ Fe	21	3.714	21	3.71			6.15	0.15
⁶¹ Fe	3	0.391	13 ^b	1.75			6.85	-1.00
⁵⁵ Co	23	3.775	23	3.78			5.35	-0.40
⁵⁶ Co	28	2.969	20	2.61			6.20	-0.78
⁵⁷ Co	34	3.296	70	4.11	8.819	0	19.4(24) ^a 13.3(11) ^a	-0.98
⁵⁸ Co	29	1.606	41	1.93			6.50	-2.23
⁵⁹ Co	38	3.090	68	3.67	10.217	0	4.3(4) ^a	-0.85
⁶⁰ Co	35	1.833	41	1.98	7.542	7/2	1.25(15)	-1.70
⁶¹ Co	24	2.499	28	2.64			6.85	-0.75
⁶² Co	12	0.920	16	1.27			7.30	-1.55
⁶³ Co	11	2.191	11	2.19			7.30	-0.30
⁶⁴ Co	8	0.953	17 ^b	1.36			7.75	-1.30
⁵⁷ Ni	22	4.374	22	4.37			5.70	0.46
⁵⁸ Ni	32	4.752	32	4.75			5.90	0.65

Table 3: continued.

Nucleus	N_d	E_d (MeV)	Fitted level and resonance data					a (MeV ⁻¹)	Δ (MeV)
			N_d	E_d (MeV)	$B + \frac{\Delta E}{2}$ (MeV)	I_0	D_0^{exp} (keV)		
⁵⁹ Ni	36	3.196	57	3.64	9.411	0	13.4(9) 12.5(9) ^a	5.90	-1.10
⁶⁰ Ni	31	4.116	45	4.54	11.394	3/2	2.0(7) ^a	6.10	0.20
⁶¹ Ni	21	2.129	21	2.13	8.045	0	13.8(9) 13.9(15) ^a	6.40	-1.24
⁶² Ni	25	3.860	47	4.46	10.631	3/2	2.10(15)	6.40	0.27
⁶³ Ni	19	2.353	19	2.35	7.117 7.238	0	16(3) 15(2) ^a	7.35	-0.52
⁶⁴ Ni	29	4.285	49	4.76				6.85	0.79
⁶⁵ Ni	20	2.520	20	2.52	6.398	0	19.6(30)	7.80	-0.20
⁵⁹ Cu	15	2.715	15	2.72				6.25	-0.45
⁶⁰ Cu	17	1.007	22	1.43				7.00	-1.75
⁶¹ Cu	35	3.092	35	3.09				6.55	-0.67
⁶² Cu	18	1.077	56	1.92				7.10	-2.00
⁶³ Cu	36	2.978	40	3.10	9.026	0	5.9(7) ^a	7.08	-0.50
⁶⁴ Cu	45	1.918	84	2.42	7.993	3/2	0.95(9)	7.25	-1.78
⁶⁵ Cu	21	2.669	51	3.36				7.70	-0.15
⁶⁶ Cu	22	1.439	22	1.44	7.166	3/2	1.30(11)	7.95	-1.35

^aRef. [54]^bLevels of similar isotope in the close neighbouring.

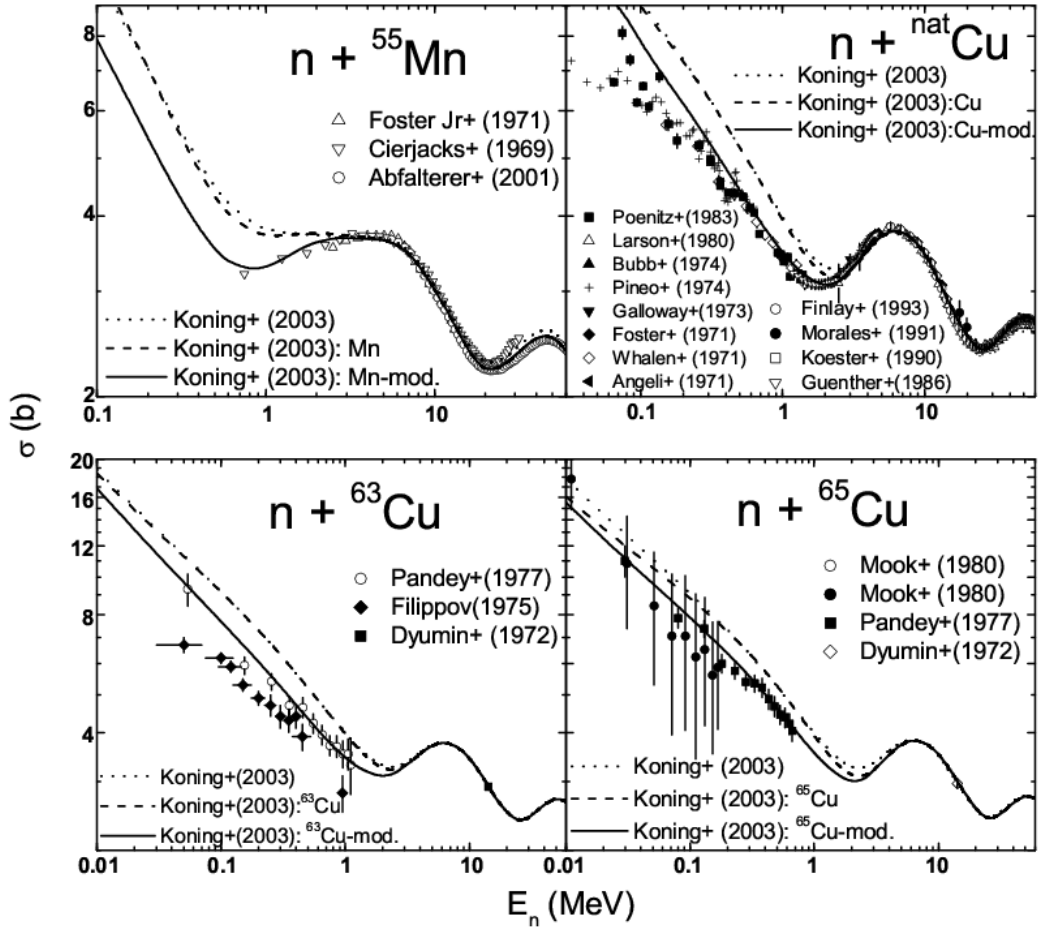


Fig. 1. Comparison of experimental and calculated neutron total cross sections for ${}^{55}\text{Mn}$ and ${}^{63,65,\text{nat}}\text{Cu}$ target nuclei, by using the global (dotted curves) and local (dashed curves) OMP parameter sets of Koning and Delaroche [22], and the changes of the latter given in Table 1 (solid curves). The experimental data are taken from the EXFOR data basis [46].

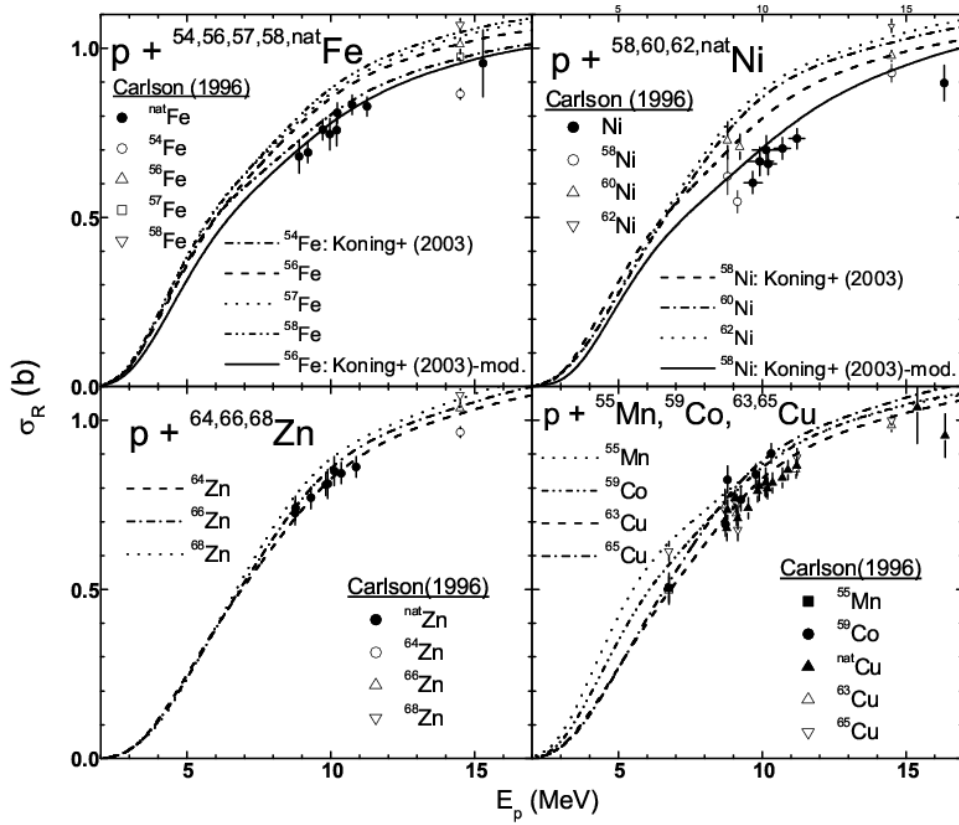


Fig. 2. Comparison of the measured [43] and calculated proton reaction cross sections on all stable isotopes of Mn, Fe, Co, Ni, Cu and Zn, by using either the local OMP predictions of Koning and Delaroche when they are available in Table 8 of Ref. [22] or otherwise their proton global OMP (dotted, dash-dotted and dashed curves) and the modified parameter set mentioned in the text for the target nuclei ${}^{56}\text{Fe}$ and ${}^{58}\text{Ni}$ (solid curves).

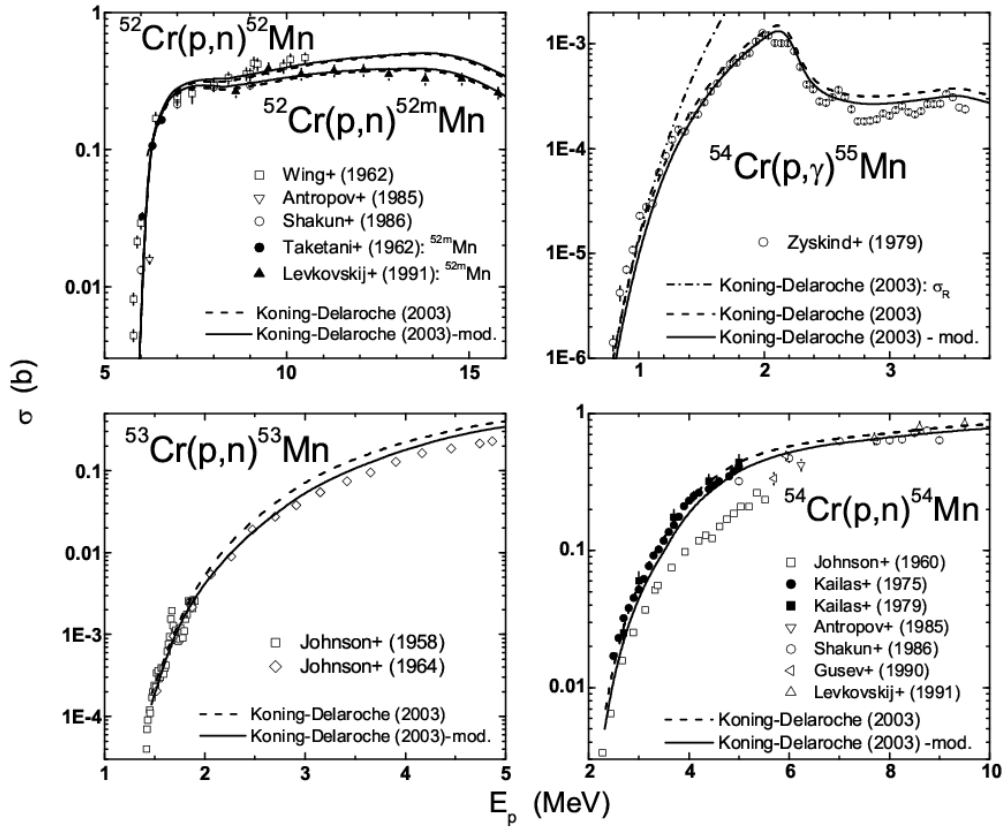


Fig. 3. Comparison of the measured [46] and calculated proton reaction cross sections (dash-dotted curve), (p, γ) and (p,n) reaction cross sections up to $E_p \sim 12$ MeV on Cr isotopes by using the OMP parameter sets mentioned for Fig. 2.

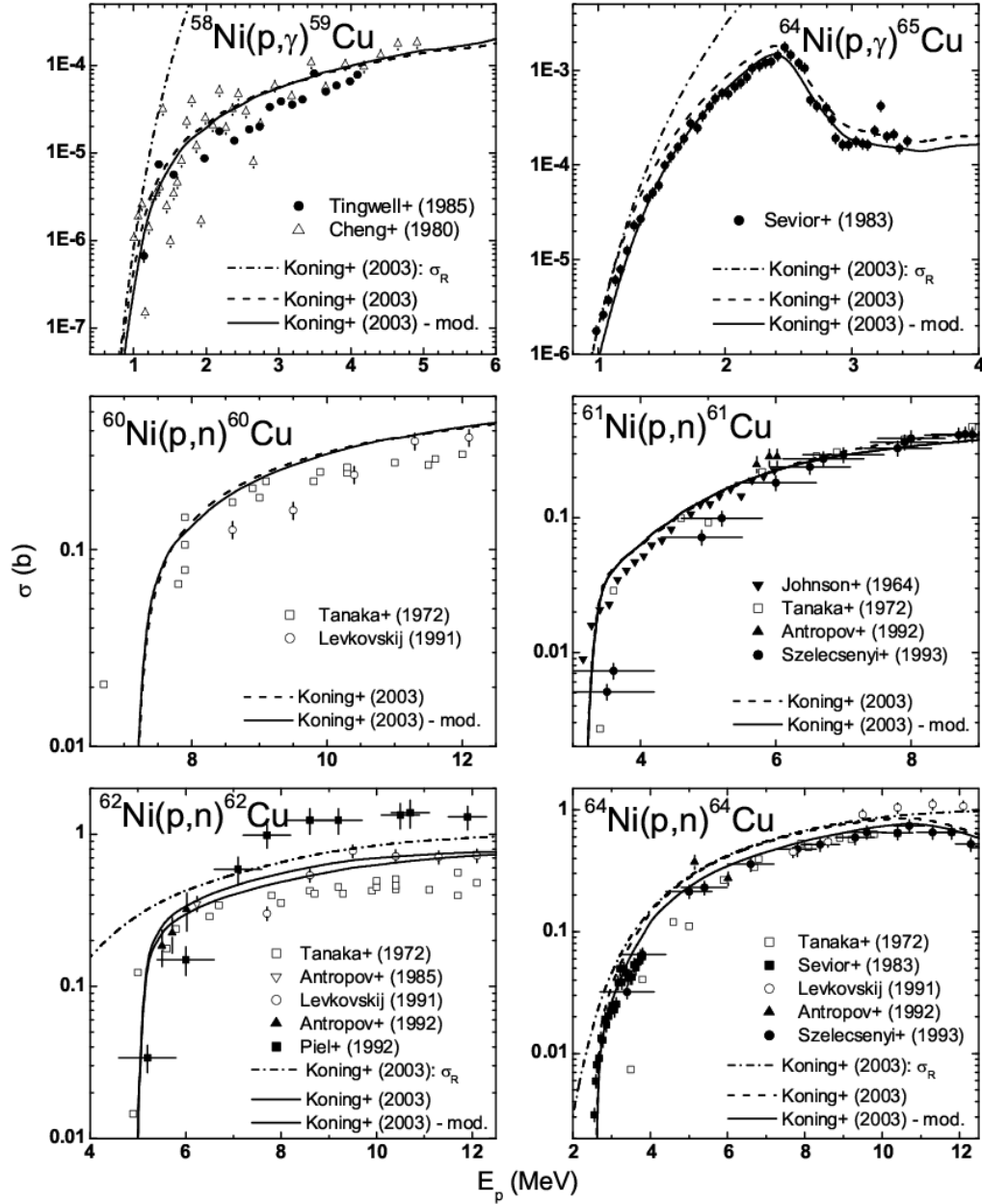


Fig. 4. As for Fig. 3, but for the Ni isotopes.

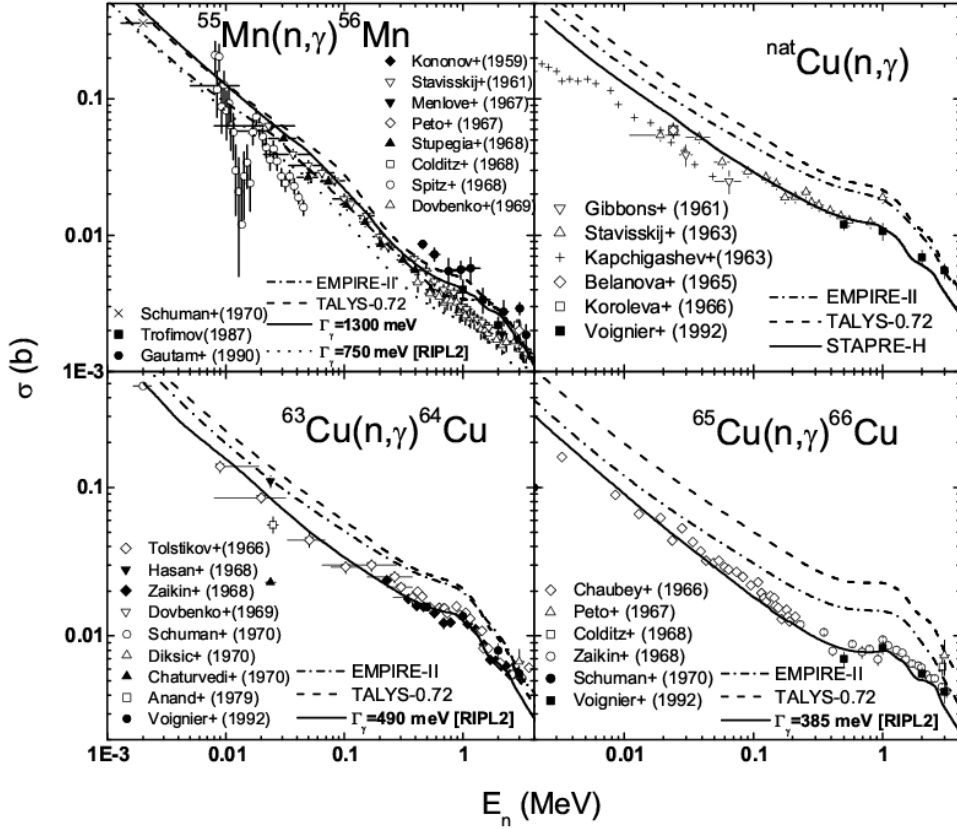


Fig. 5. Comparison of the measured [46] neutron-capture cross sections of ^{55}Mn and $^{63,65,\text{nat}}\text{Cu}$ target nuclei, for incident energies up to 3–4 MeV, and calculated values by using the computer codes TALYS-0.72 (dashed curves) and EMPIRE-II (dash-dotted curves) with default global parameters, and the local analysis with γ -ray strength functions $f_{E1}(E_\gamma)$ within the EDBW model corresponding to either the experimental [24] average s -wave radiative widths $\Gamma_{\gamma 0}$ (dotted curves), or $\Gamma_{\gamma 0}$ values corresponding to a fit of experimental neutron capture data (solid curves).

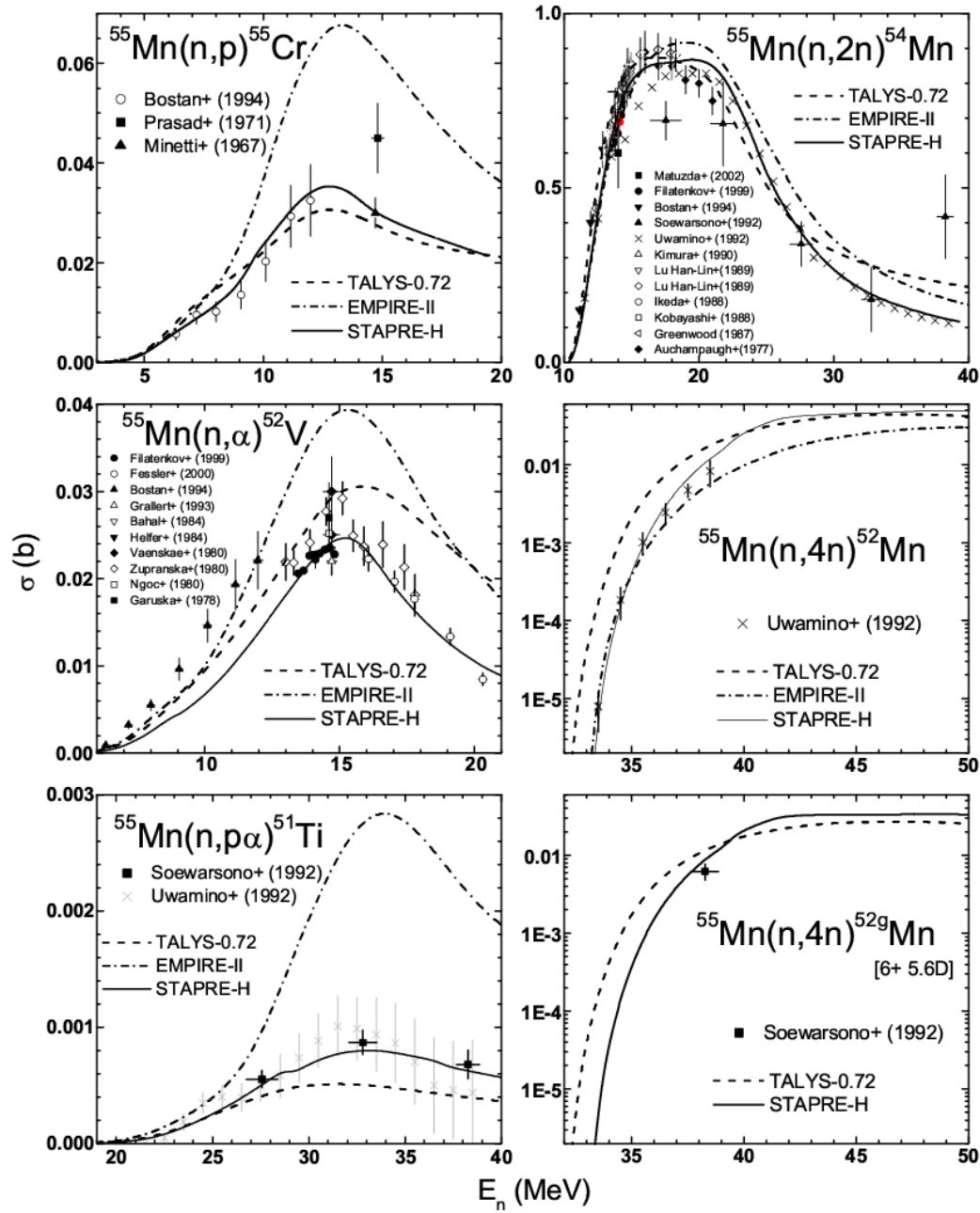


Fig. 6. Comparison of measured [46] and calculated neutron-activation cross sections for the target nucleus ^{55}Mn , by using the computer codes TALYS-0.72 (dashed curves) and EMPIRE-II (dash-dotted curves) with default global parameters, and STAPRE-H (solid curves) with the local parameter set given in this work.

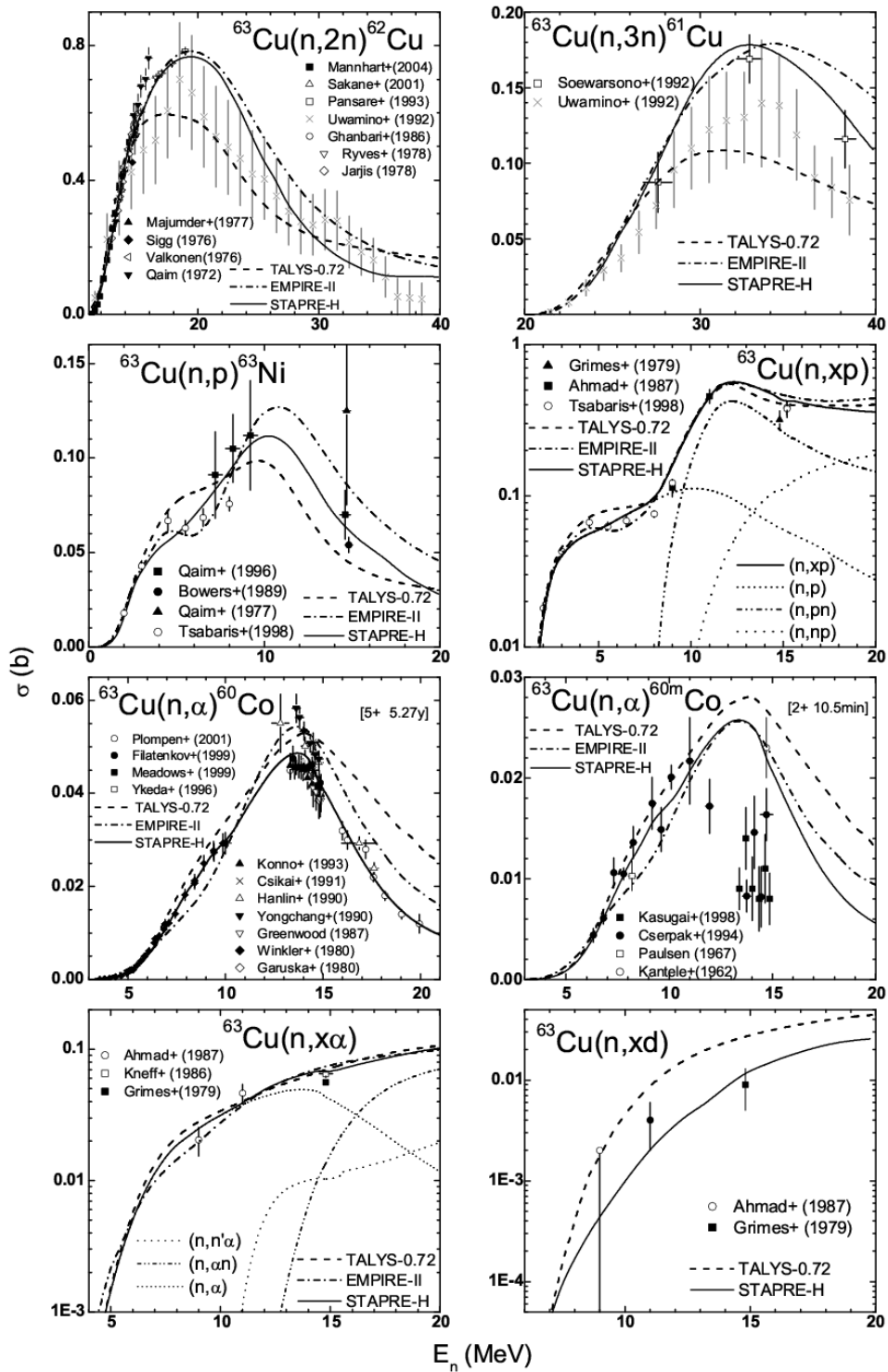


Fig. 7. As for Fig. 6, but for the target nucleus ^{63}Cu .

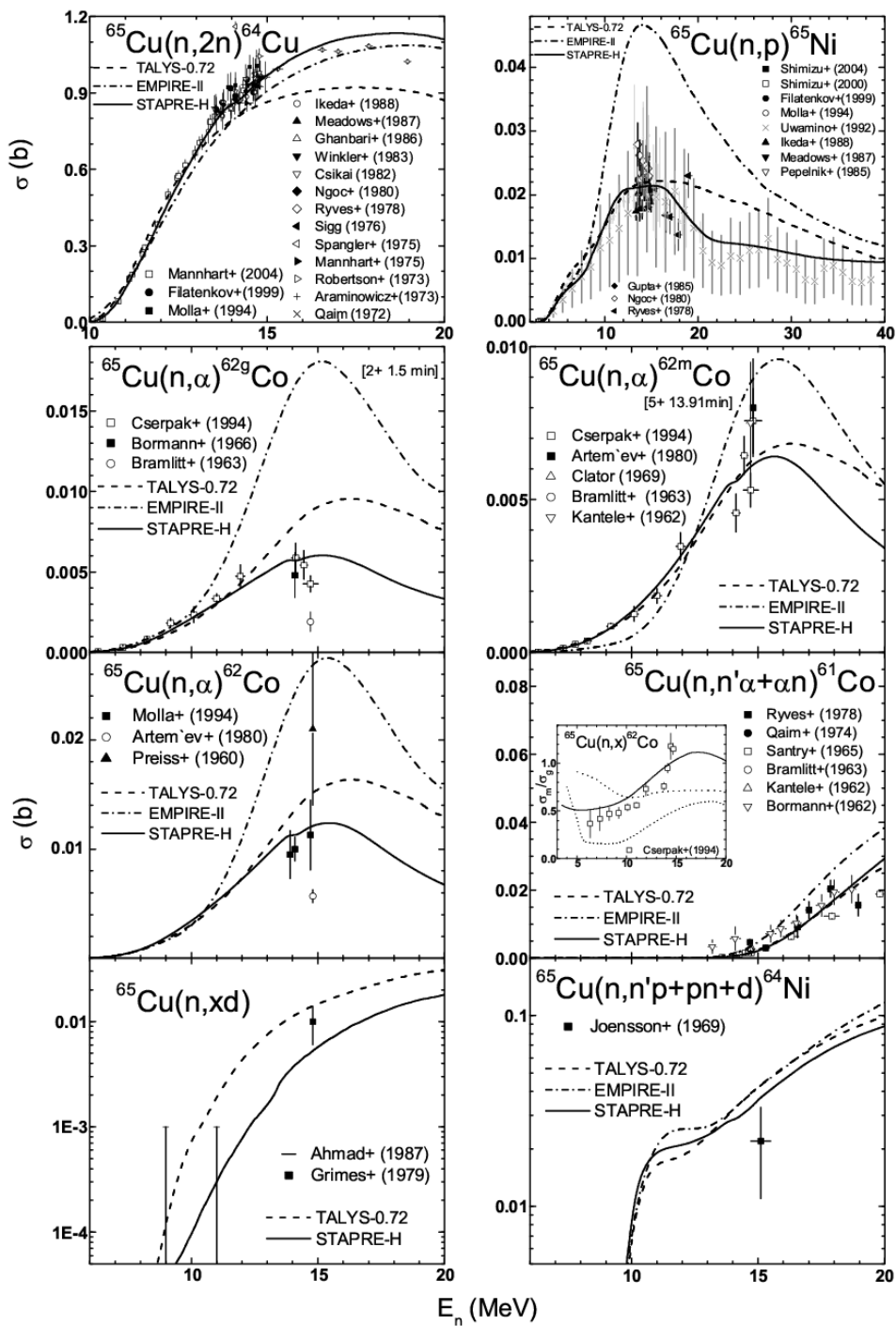


Fig. 8. As for Fig. 6, but for the target nucleus ^{65}Cu .

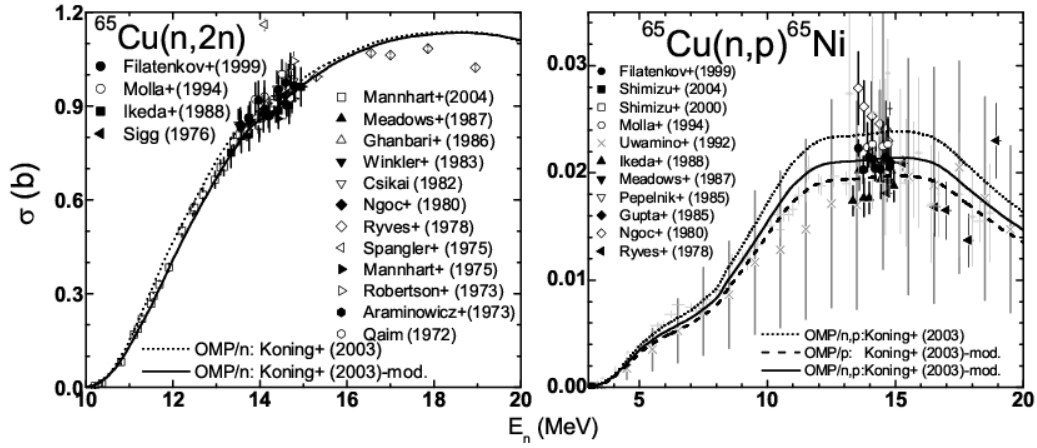


Fig. 9. Comparison of measured [46] and calculated cross sections within the local approach for the (n,2n) and (n,p) reactions on the target nucleus ^{65}Cu , by using the OMP parameter sets of Koning and Delaroche [22] (dotted curves), and corresponding changes for the proton OMP (dashed curve) and neutron OMP (solid curves).

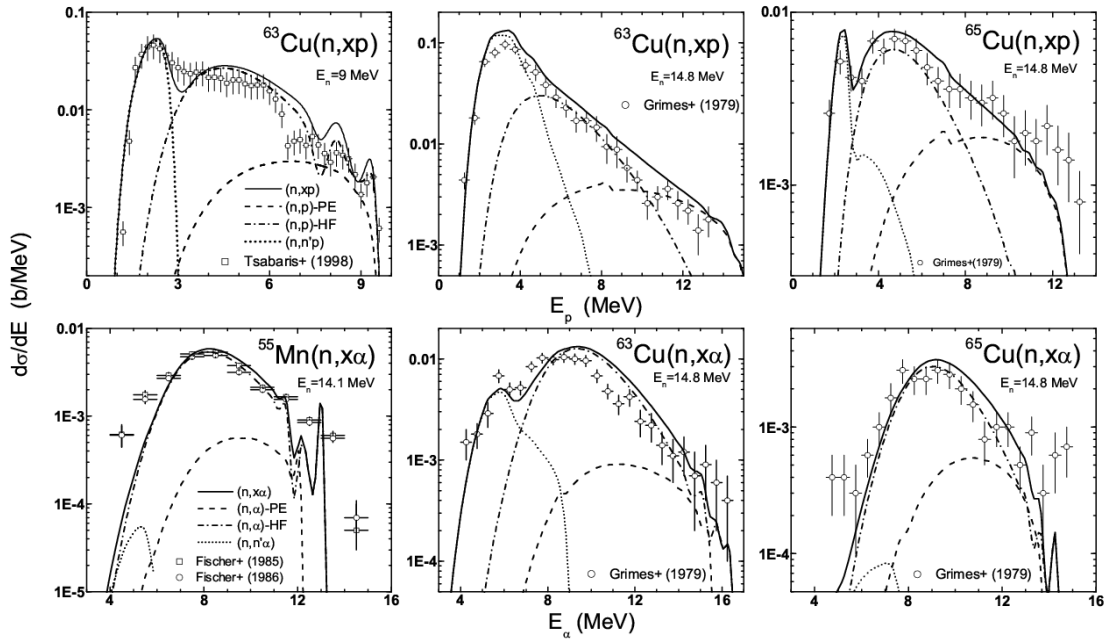


Fig. 10. Comparison of measured [46,48,62,63,64] angle-integrated proton and α -particle emission spectra from 9, 14.1 and 14.8 MeV neutron-induced reactions on the ^{55}Mn and $^{63,65}\text{Cu}$ nuclei and calculated values within the local approach for the PE emission (dashed curves), statistical first- (dash-dotted curves) and second-emitted particles (dotted curves) from equilibrated compound nuclei, and their sum (solid curves).

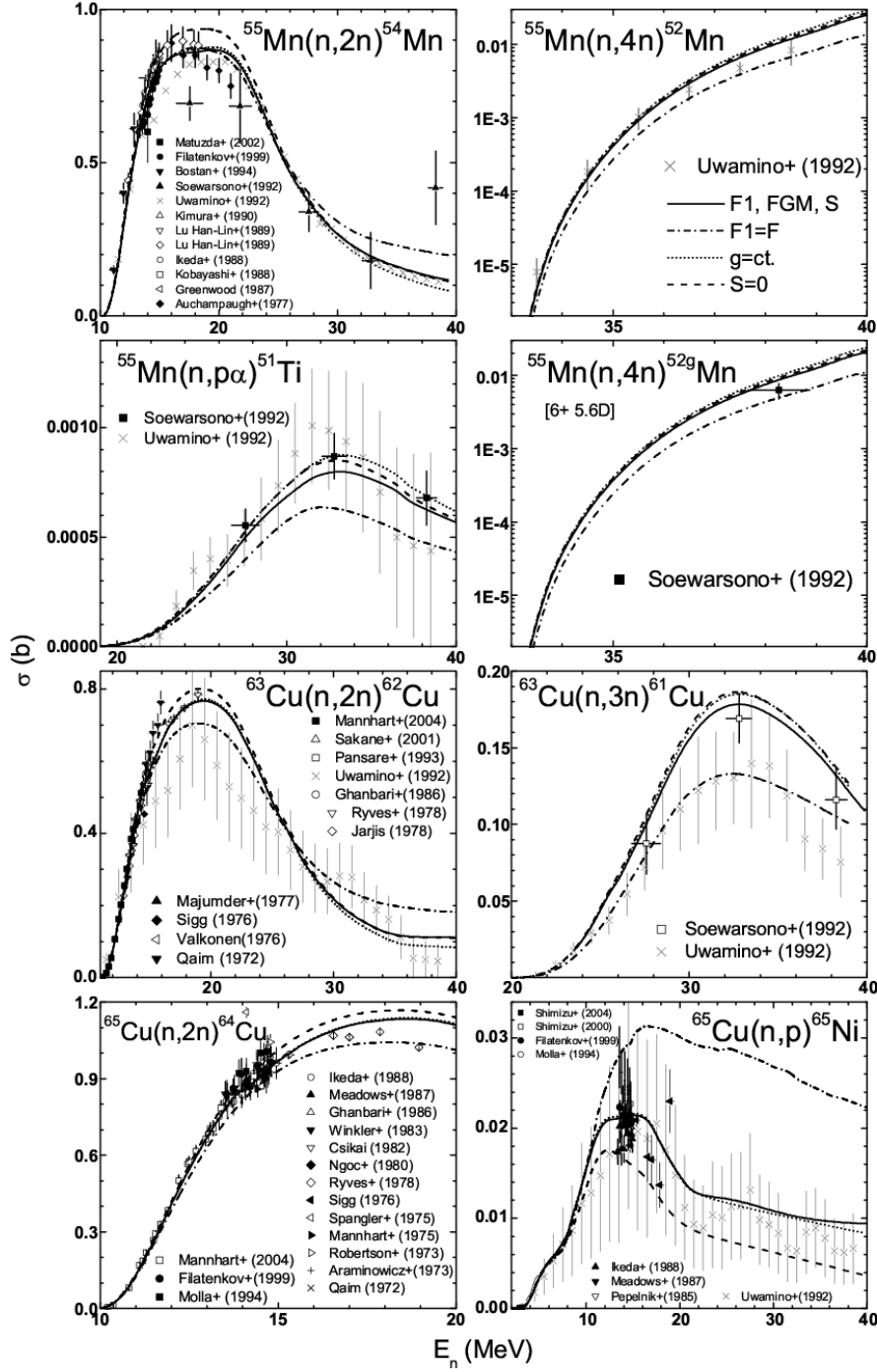


Fig. 11. Comparison of measured [46] neutron-activation cross sections for the target nuclei ^{55}Mn and $^{63,65}\text{Cu}$ up to 40 MeV, and calculated values with the local parameter set given in this work (solid curves) except for replacement of either the local-density Fermi energies $F_1(R_l)$ with the Fermi energy central value F (dash-dotted curves), or the average energy-dependent s.p.l. densities with the constant value $g(F)$ (dotted curves), as well as for removal of the shell correction S in the PSD composite formula (dashed curves).

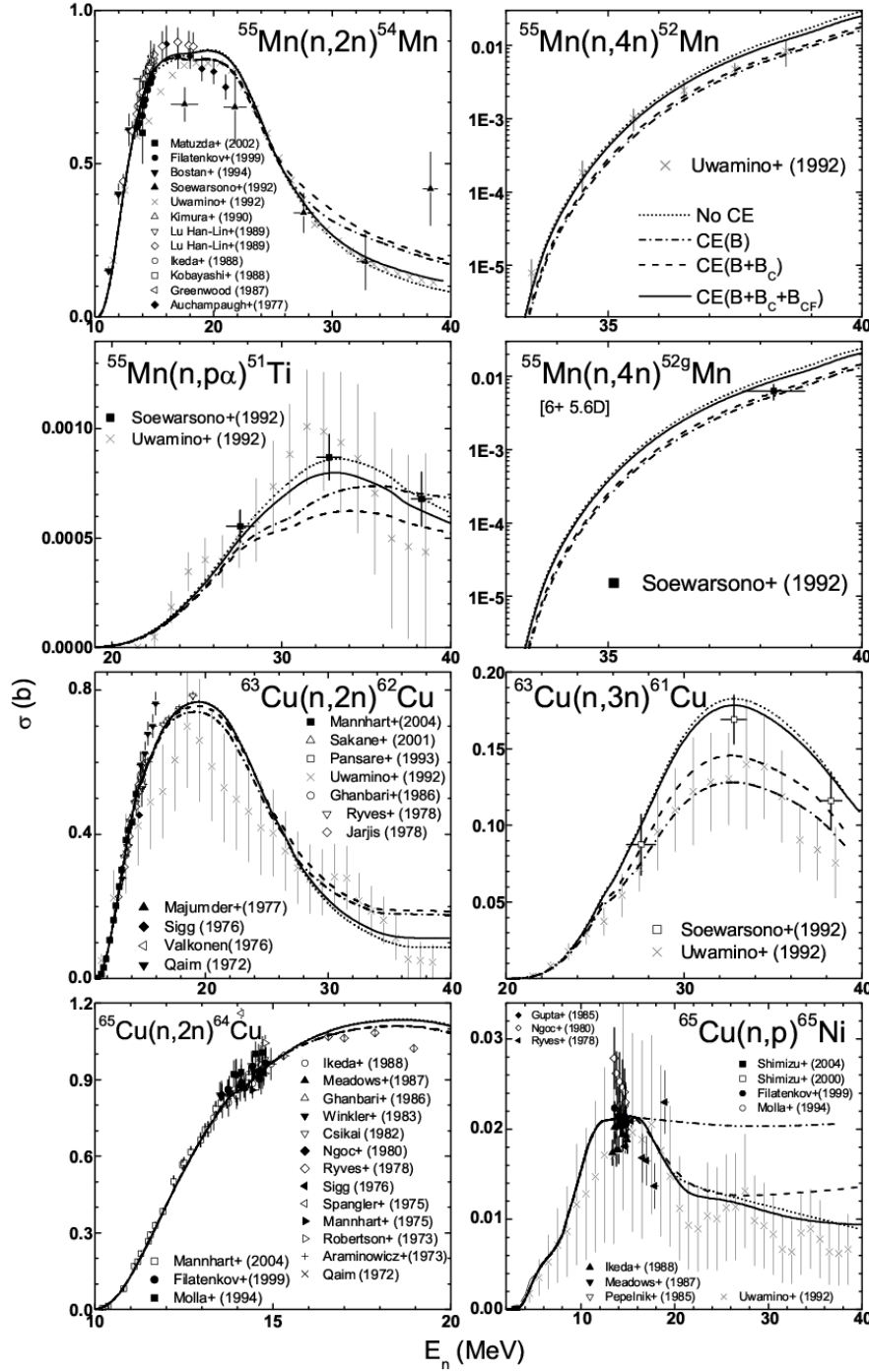


Fig. 12. As for Fig. 11, but for removal of the 'continuum effect' (CE) of the s.p.l. density within the particle-hole state density calculation (dotted curves), and taking into account for this effect the nucleon binding energy B either alone (dash-dotted curves) or together with the Coulomb barrier B_C (dashed curves), while the solid curves correspond to consideration of also the centrifugal barrier B_{CF} .